

An investigation on pyrite floatability using stable micro-nanobubble-assisted flotation

Hassan Heidari ¹, Asghar Azizi ¹, Ahmad Hassanzadeh ^{2,3}

¹ Faculty of Mining, Petroleum & Geophysics Engineering, Shahrood University of Technology, Shahrood, P.O. Box: 3619995161, Iran

² Department of Geoscience and Petroleum, Faculty of Engineering, Norwegian University of Science and Technology, 7031 Trondheim, Norway

³ Maelgwyn Mineral Services Ltd, Ty Maelgwyn, 1A Gower Road, Cathays, Cardiff, CF24 4PA, United Kingdom

Corresponding author: aazizi@shahroodut.ac.ir (A. Azizi)

Abstract: This study critically examines the impact of micro-nanobubble (MNB)-assisted flotation on pyrite recovery in bulk ore, and clarifies the intricate relationship between pyrite and its associated ore. The physicochemical properties of MNBs and the interaction mechanisms between xanthate collector and pure pyrite mineral were evaluated using advanced analytical techniques, including Dynamic Light Scattering (DLS), Field-Emission Scanning Electron Microscopy coupled with Energy-Dispersive X-ray Spectroscopy (FESEM-EDX), and Ultraviolet-Visible Spectroscopy (UV-Vis), in the absence and the presence of MNBs. MNBs were created through hydrodynamic cavitation, and their characteristics revealed a size increase from 600 nm to 3 μm over 25 days. Notably, the zeta potential measurements indicated an increase from -2.5 to 0 mV at a constant pH of 8, correlating with the geometric mean size of MNBs coarsening from 600 nm to 2-3 μm . The FESEM and EDS analyses disclosed that ultrasonic treatment effectively dispersed ultrafine surface coatings on pyrite particles, increasing iron and sulfur purity by 8% and 6%, respectively, and significantly reducing surface oxygen by 53%. Micro-flotation and batch rougher kinetic flotation experiments were conducted with and without MNBs, leading to a 7% and 8% improvement in recovery for pyrite mono-minerals (-105+53 μm) and its ore ($d_{80}=150 \mu\text{m}$), respectively. The sorption behavior of sodium isopropyl xanthate (SIPX) collector on the particle surface was also investigated at various concentrations (ca. 10-160 μM) in the presence and absence of stable MNBs and demonstrated that the presence of MNBs resulted in a 1.6-fold increase in collector absorption on the pyrite surface, confirming the findings obtained from micro-flotation. Moreover, adsorption behavior is up to 1.3 times compared to the scenario without MNBs. The adsorption process was controlled by a pseudo-second-order model, indicating a chemical sorption mechanism.

Keywords: pyrite recovery, flotation, ultrasonic treatment, SIPX collector, adsorption mechanism

1. Introduction

Pyrite, a common sulfide mineral, is often associated with copper ores and can significantly impact the efficiency of the flotation process (Hassanzadeh and Hasanzadeh, 2016; Hassanzadeh and Karakaş, 2017; Yenial-Arslan et al., 2023). The presence of pyrite can result in reducing copper recovery and increasing reagent consumption, presenting challenges for the economical extraction of copper from its ore. The flotation process relies on the differences in the surface properties between copper minerals and gangue minerals to achieve separation (Bilal et al., 2022). Different reagents are employed to selectively coat the surfaces of copper minerals with hydrophobic molecules, enabling them to attach to air bubbles and rise to the surface. In contrast, the gangue minerals remain in the aqueous phase (Feng et al., 2022). However, the presence of pyrite complicates this process, as it exhibits similar surface properties to copper minerals, leading to poor selectivity and low recovery.

The presence of gold in pyrite, although rare, can be economically significant (Altun et al., 2010). The recovery of gold from pyritic minerals is an efficient process, particularly for copper flotation plants

aiming to maximize pyrite recovery in copper concentrates. Several studies have focused on enhancing gold recovery from pyrite-rich ores to increase the economic value of operations (Forrest et al., 2001; Qin et al., 2021; Allard et al., 2022; He et al., 2023). One of the main challenges in the flotation of copper ores containing precious metals is the use of lime as a depressant. For instance, Panayotov and Panayotova (2023) successfully replaced lime with a catholyte (a solution obtained from the electrolysis of water), resulting in increased precious metal content in copper concentrates. Their results demonstrated an increase of 68.41 g/Mg Au and 61.23 g/Mg Ag, along with a 3% increase in copper recovery compared to conventional methods. Therefore, maximizing pyrite recovery in copper concentrates can significantly enhance the overall economic value of operations (Dunne, 2005).

Recent studies have highlighted the potential of MNBs in enhancing the flotation process by interacting with minerals and reagents, potentially improving the selectivity and recovery of valuable minerals (Pourkarimi et al., 2021). These ultrafine gas bubbles, characterized by high solubility, extended residence times, and large interfacial areas (Tao, 2022; Nazari et al., 2022), have been found to facilitate the formation of stable mineral aggregates, aiding in the attachment of collector molecules and air bubbles to mineral surfaces (Sobhy and Tao, 2013; Taghavi et al., 2022; Shadman et al., 2023).

In the absence of MNBs, xanthate collectors interact with various adsorption sites on the surface of pyrite, with the adsorption mechanism involving complex interactions influenced by pH levels and the presence of other reagents. For instance, a previous research study by Wang and Forssberg (1991) demonstrated that the adsorption mechanism involved the formation of stable Fe (III)-xanthate compounds on the pyrite surface, significantly influencing pyrite flotation behavior with xanthates as collectors. Gu et al. (2010) found that the collector DLZ exhibited chemical adsorption on the chalcopyrite surface, while only physical adsorption occurred on the pyrite surface, as demonstrated using infrared spectroscopy analysis. Bulut et al. (2021) showed that the adsorption mechanism entailed the substitution of positively charged iron hydroxide species on the pyrite surface with neutral iron hydroxide-xanthate complexes, making pyrite hydrophobic and enhancing the negative zeta potential of pyrite. Moreover, Deng et al. (2020) demonstrated that the collector adsorption mechanism on the pyrite surface involved the formation of copper xanthate and iron xanthate, resulting in the production of both cuprous xanthate and cupric xanthate on the pyrite surface. Additionally, Otsuki and Zhao (2018) proposed a dual mechanism for PAX collector adsorption on the pyrite surface, suggesting distinct adsorption sites for different collectors and the formation of additional adsorption sites on top of the initial layer of collectors, facilitating further adsorption. A recent study by Wu et al. (2023) provided new insights into the impact of micro-nano bubbles on collector adsorption on the pyrite surface. They concluded that the presence of nano-bubbles enhanced sodium isopropyl xanthate (SAX) adsorption on pyrite due to stronger hydrophobic interactions, potentially increasing SAX adsorption capacity.

As discussed, the existing literature provides limited information on the separation of iron-bearing minerals and ores using froth flotation processes in various commodities. This study aims to comprehensively investigate the impact of MNBs on the floatability of pyrite and its gold-bearing ore. Additionally, our goal is to clarify the relationship between the adsorption of the SIPX collector on the pyrite surface in the presence and absence of micro-nanobubbles.

2. Materials and methods

2.1. Pyrite mineral, bulk sample, and chemical reagents

High-purity pyrite crystal samples for micro-flotation and adsorption experiments were obtained from the Midok copper mine in Kerman, Iran. The samples underwent a three-stage process including manual sorting, jaw crushing (Jaw crusher, Fritsch 01.703, Idar-Oberstein, Germany), and disc milling (Disk Mill PULVERISETTE 13, Fritsch Co., Germany) for separation and comminution. Subsequently, they were classified into the -105+53 μm size fraction using the wet method with standard Taylor sieves. To prevent oxidation of the particle surfaces, the pure pyrite samples were promptly transferred into plastic containers. After saturation with nitrogen gas and sealing the lids tightly, the containers were stored in a refrigerator at a temperature of -4°C . The pure pyrite sample was analyzed using the X-ray Diffraction (XRD, ASENWARE, AW-XDM300, China) method as shown in Fig. 1. As it can be seen from the results presented, pyrite exhibits a high level of purity.

The bulk samples comprised 100 kg of a representative sample of sulfide copper-gold ore from the feed of the ball mill at the copper processing plant in Qaleh-Zari (Birjand, Iran). The Qaleh-Zari mine, situated in the city of Birjand, is recognized as a significant mining center in Iran due to its copper-gold reserves and other by-product minerals (Seyedi et al., 2023). The bulk samples underwent two stages of crushing and milling using a jaw crusher and a disc mill to achieve a particle size of $d_{80}=150\ \mu\text{m}$. The particle size distribution results of the bulk sample are depicted in Fig. 2.

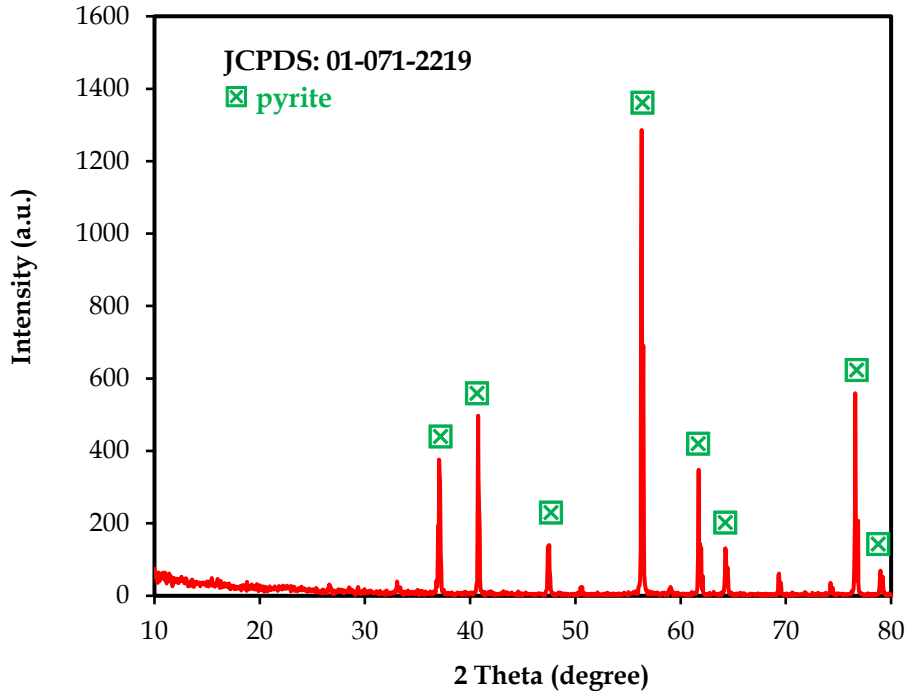


Fig. 1. XRD diffractogram of the pyrite mineral

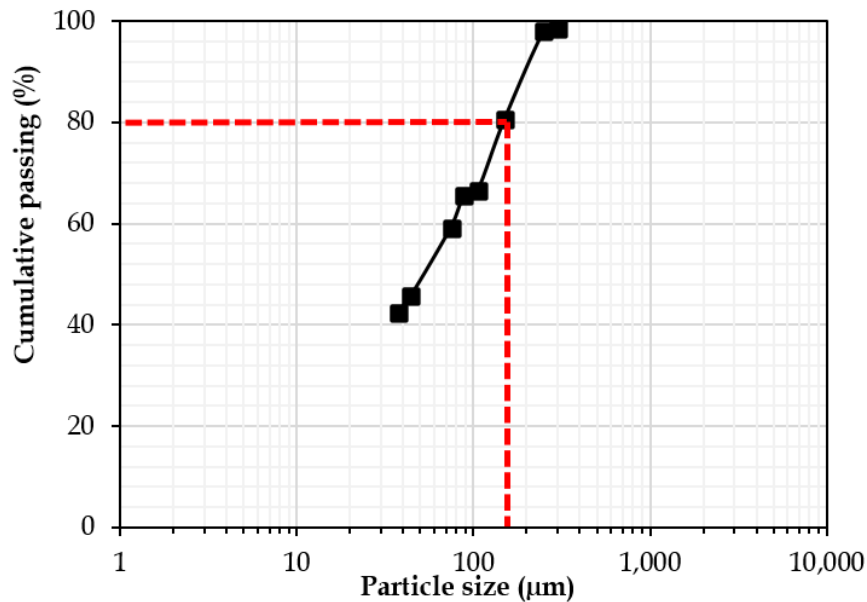


Fig. 2. Particle size distribution of the bulk sample utilized as the flotation feed

Chemical analysis of the bulk sample using Thermo Elemental's SOLAAR S Series (Waltham, MA, USA) atomic absorption spectroscopy (AAS) showed that the copper content was 0.79%; and the iron content was 4.21%, respectively. Furthermore, the XRF analysis results of the bulk sample are detailed in Table 1.

Table 1. The elemental composition of the bulk sample

Chemical composition	SiO ₂	Al ₂ O ₃	Fe ₂ O ₃	CaO	Na ₂ O	K ₂ O	MgO
Content (wt. %)	63.751	11.243	6.681	4.244	0.704	2.823	1.921
Chemical composition	TiO ₂	MnO	P ₂ O ₅	SO ₃	CuO	PbO	LOI*
Content (wt. %)	0.44	0.378	0.165	2.670	0.900	0.368	3.83

LOI: Loss on ignition

The chemical reagents used in this study included the sodium isopropyl xanthate collector (SIPX, C₃H₇OCS₂Na, 158.2 g/mol) and the methyl isobutyl carbinol frother (MIBC, C₆H₁₄O, 102.17 g/mol), sourced from Co-Polymer Company (Isfahan, Iran). In micro-flotation tests, only the SIPX the collector was used as the chemical reagent to minimize particle-agent interactions. Adjustment of suspension pH was carried out using analytical-grade sodium hydroxide (NaOH) and hydrochloric acid (HCl) provided by Merck GmbH. For all experiments, including micro-flotation, adsorption, and bulk flotation tests, a significant amount of distilled water (DW) was prepared as the stock solution with and without micro-nanobubbles at a temperature of 25±3°C and pH 8. The elemental analysis of the distilled water was conducted using the Inductively Coupled Plasma optical emission spectrometer (ICP-OES, Espectro Arcos, AMETEK Model, USA) method. The results of the chemical analysis of the distilled water are presented in Table 2. The electrical resistivity of the distilled water stock solution was 18 mΩ.

Table 2. Results of the ICP-OES chemical analysis for the distilled water

Element	Al	Ba	Ca	K	Mg	Mn	Na	Pb	S	Sr	Zn
Content (ppm)	0.009	0.004	2.56	0.44	0.47	0.006	0.8	0.025	0.4	0.08	0.004

2.2. of micro-nanobubbles and detection

This research utilized a two-phase micro-nano bubble (MNB) generator developed at Shahrood University of Technology in Iran to generate MNBs through the hydrodynamic cavitation technique. The experimental apparatus comprised a horizontal centrifugal pump rated at 750 W, capable of operating between a minimum pressure of 25 kPa and a maximum of 50 kPa, along with a 20 L feed tank and a Venturi tube featuring a 3 mm internal diameter. Micro-nano bubble (MNB) generation occurs as follows: the centrifugal pump initiates a swift water flow, which lowers pressure and facilitates gas bubble formation within the liquid. As the flow accelerates through the Venturi tube, pressure further decreases, enhancing bubble formation. Continuous air mixing with saturated water also aids in producing smaller bubbles, leading to the creation of MNBs. To achieve a high concentration of micro-nanobubbles in distilled water, a specially designed generator was employed. By circulating water in a closed-loop circuit for 5 min from the pump to the tank, continuous mixing of air with the saturated aqueous was utilized for MNB production (Taghavi Zinjenab et al., 2024). The MNB generator device consisted of three main components: an air inlet, pressure application, and a pressure reduction zone for gas release. The introduction of gas improved cavitation efficiency and MNB generation, with the capability to handle multiple gases for a variety of MNBs. The formation of MNBs occurs during rapid pressure changes in the cavitation process, leading to bubble nucleation. The stability of these bubbles is influenced by factors such as surface tension, bubble size, and the presence of surfactants. Over time, the bubbles may coalesce or dissolve, depending on the surrounding environmental conditions.

In this study, we used two types of water: one without micro-nanobubbles and another saturated with micro-nanobubbles. This approach allowed us to investigate the simultaneous effects of micro and nanobubbles in the flotation process. Additionally, the study progressed from mono-mineral tests to bulk flotation. The laboratory-scale MNB generator setup is depicted in Fig. 3.

In this study, we assessed the stability and size distribution of MNBs using dynamic light scattering (DLS, Litesizer 500 model, Anton Paar Co., Australia). The standard for measuring bubble size using DLS, as defined in 'BS ISO 13320-20,' ensures that our assessments of MNBs' size distribution are reliable and consistent with established protocols. DLS is a versatile technique that not only measures particle size in a solution but also determines the zeta potential of particles. It analyzes the intensity fluctuations

of scattered light by particles (or MNBs) in suspension. Additionally, it can assess the motion of charged particles under an applied electric field using the Electrophoretic Light Scattering (ELS) method (Olszok et al., 2020; Kyzas et al., 2021; Nazari et al., 2022; Nikouei Mahani et al., 2024).

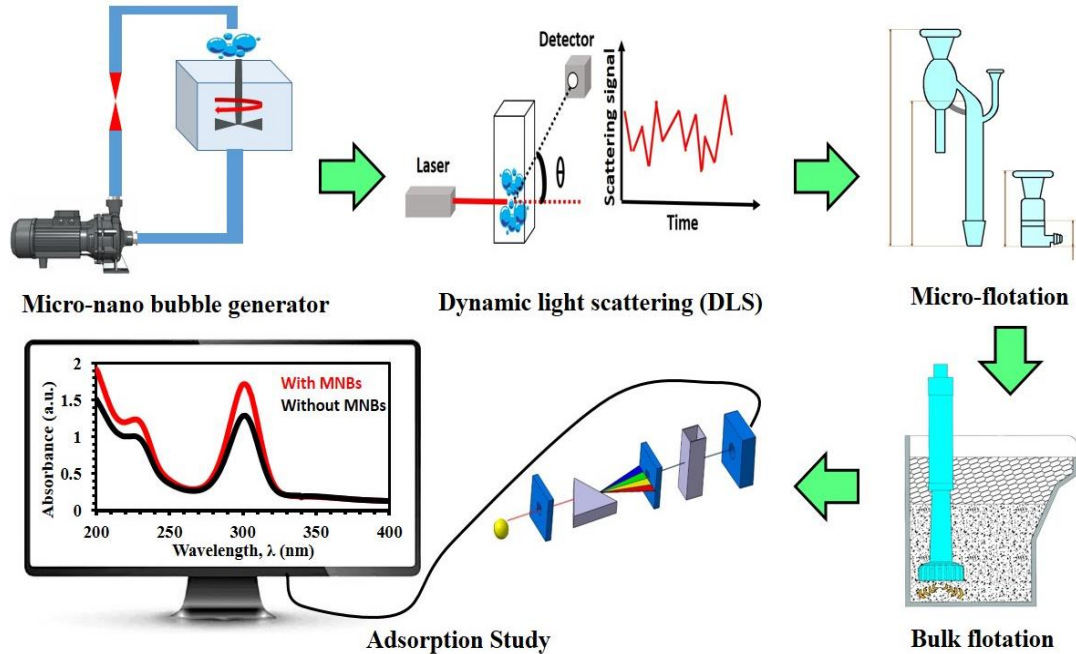


Fig. 3. A schematic diagram of the micro-nanobubble generator and the various stages of experiments in the present study

2.3. Ultrasound-based pretreatment and characterization by FESEM images

The ultrasonic treatment was used to enhance the sorption process and decrease the surface coating and oxidation of pyrite particles. Before conducting adsorption and micro-flotation tests, it was crucial to subject pyrite samples to ultrasound pretreatment (Ozun et al., 2019; Hassanzadeh et al., 2021; Kruszelnicki et al., 2022). In this study, pyrite samples (-105+53 μm) were exposed to a 30 kHz frequency and 80% power for 5 min in a 2.75 dm³ ultrasonic bath (Elmasonic P units, P30H model, Elma, Germany). The surface morphology was analyzed using Field emission scanning electron microscopy (FESEM, Sigma 300-HV model, Zeiss Co., Germany), and the elemental composition was examined through Energy-Dispersive X-ray Spectroscopy (EDS).

2.4. Micro-flotation and adsorption tests

Pure pyrite flotation tests were conducted in a modified Hallimond tube equipped with a 16 μm porous ceramic plate and a Teflon-coated magnetic rod for pulp mixing. A narrow throat was used to regulate the particle transfer path to the concentrate collection bulb, ensuring frother-free micro-flotation tests and minimizing mechanical entrainment of particles not attached to air bubbles (Cao and Liu, 2006). For the micro-flotation tests, 1 g of pyrite (-105+53 μm) was mixed with MNB-containing water and subjected to ultrasonic waves for 5 min. The pH of the mixture was adjusted using NaOH and HCl. Subsequently, SIPX collector was introduced to the pulp, agitated for 2 min, and then transferred to the modified Hallimond tube for flotation. The mass recovery of the pure mono-mineral was calculated after flotation. The influence of SIPX concentration at six levels (i.e., 0, 25, 50, 75, 100, and 175 μM) with and without MNBs on pyrite floatability was evaluated. Each micro-flotation experiment was replicated four times and the results were presented with experimental error bars.

The study employed the UV spectroscopy (UV-Vis, Shimadzu UV 1800, Japan) method to investigate the xanthate collector's mechanism on pyrite's surface. A calibration curve was plotted using SIPX collector solutions at different concentrations (ca. 10-160 μM) with and without MNBs, as depicted in Fig. 4. The solutions were adjusted to pH 9 and stirred for 20 min at room temperature. The absorption

at 301 nm was measured using a UV spectrophotometer, revealing a linear relationship (Absorbance = $0.0113 C_{\text{SIPX}} - 0.0215$, $R^2 = 0.9994$) between SIPX concentration and absorption changes at $\lambda = 301$ nm, consistent with previous studies (Agorhom et al., 2013; Han et al., 2020; Heidari et al., 2024).

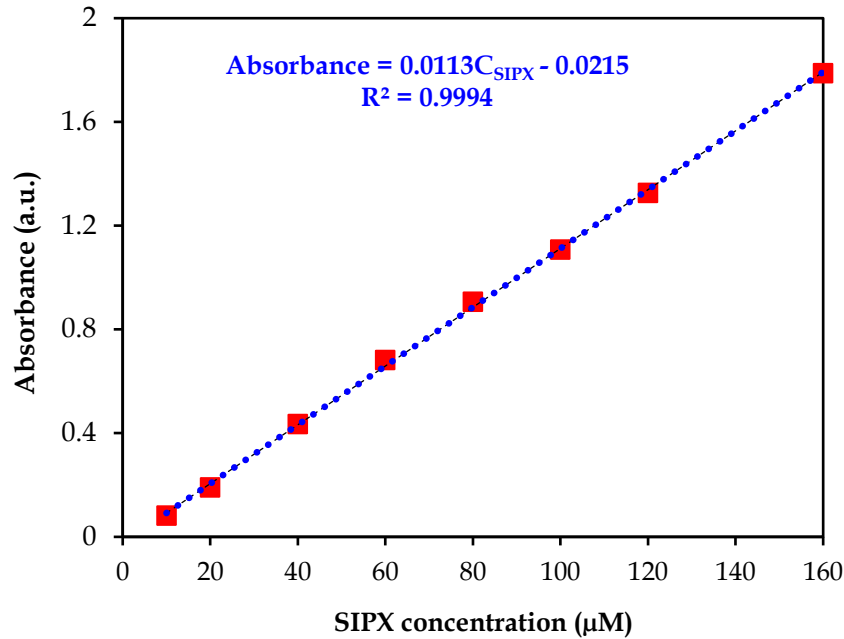


Fig. 4. Absorption intensity plot for SIPX collector solution at designated concentrations (The laboratory conditions included distilled water, a pH of 9, sodium isopropyl xanthate (SIPX) collector at concentrations ranging from 10 to 160 μM , and were conducted at room temperature of $25 \pm 2^\circ\text{C}$)

The adsorption tests were conducted on pure pyrite at $25 \pm 2^\circ\text{C}$ with two replications using the gravimetric method. To prepare a specific concentration of SIPX stock a certain amount of SIPX collector was dissolved in distilled water. Subsequently, various SIPX collector concentrations (ca. 10-160 μM) were prepared and added to 0.5 g of pyrite in a 50 mL beaker, with the pH adjusted to 9 ± 0.3 . After mixing and filtration, the collector concentrations were measured at 301 nm using a UV spectrophotometer. The tests were replicated twice to determine the measurement error bars, and the adsorption capacity was calculated using Eq. (1).

$$q_e = \frac{V(C_0 - C_i)}{m} \quad (1)$$

where q_e is the adsorption capacity of SIPX on the chalcopyrite surface (mg/g); V is the suspension volume (L); C_0 and C_i are the SIPX concentrations in the solution before and after reaction with the chalcopyrite surface, respectively (μM); and m is the mass of the mineral sample (g).

2.5. Bench scale flotation tests

Bulk rougher copper flotation tests were conducted in a 2.5 dm³ laboratory Denver® flotation cell under constant conditions: impeller speed of 900 rpm, 30% (w/w) solid percentage, 40 g/Mg SIPX collector, 90 g/Mg MIBC frother, and pH 9. These values were determined through extensive test works recommended by the Qaleh-Zari beneficiation plant's metallurgical laboratory. Deionized water with 18 M Ω electrical conductivity was used to prevent impurities. Each experiment involved adding 860 g of copper ore sample ($d_{80} = 150 \mu\text{m}$) to the cell with deionized water, followed by mixing and pH adjustment to 9 using lime. After adding the SIPX collector and MIBC frother to the flotation cell, the air inlet valve was opened to initiate the flotation kinetic tests. This step allows air to flow into the cell, creating air bubbles that are essential for the flotation process, facilitating the separation of particles. The samples were taken at intervals, and water was added to maintain a constant pulp level. Each experiment was repeated twice, both with and without MNBs, at room temperature ($25 \pm 3^\circ\text{C}$). The

concentrate and tailings were dried overnight at 70°C and sent for chemical analyses at the atomic absorption laboratory of Shahrood University of Technology.

3. Results and discussions

3.1. Properties of micro-nanobubbles

Fig. 5 shows the distribution of micro-nano bubble sizes (MNBs) for 0 to 25 days. The cumulative passing percentage is displayed as a function of the bubble diameter (μm). The results indicate that bubble sizes increase over time. On the first day, most bubbles are below 1 μm , and over time, this size increases to 2-3 μm , eventually reaching about 5 μm by day 25. These changes are likely due to the coalescence of bubbles (Nazari and Hassanzadeh, 2020; Khoshdast et al., 2021) and indicate the stability of micro-nano bubbles over time.

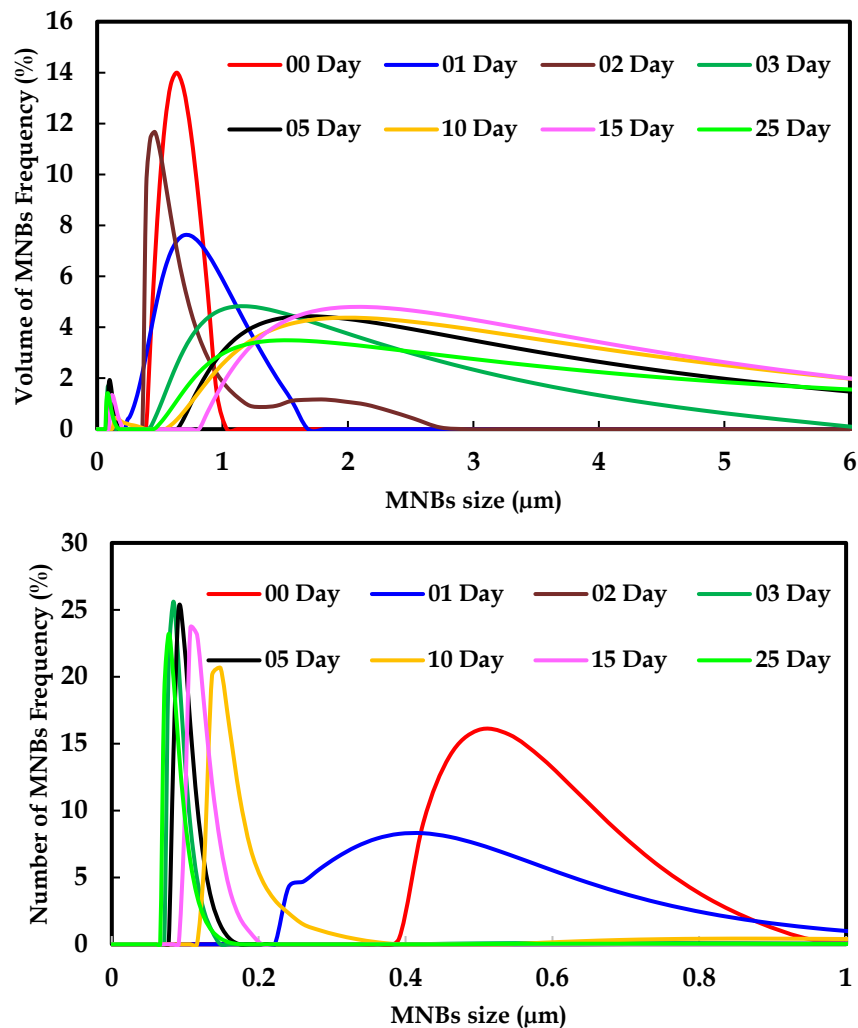


Fig. 5. Bubbles' size distribution based on different conditions related to (a) volume and (b) number of micro-nanobubbles (MNBs) (Laboratory Conditions: Distilled water, pH = 8, free of chemical reagents, and room temperature of $25\pm 2^\circ\text{C}$)

Fig. 6 depicts the bubble zeta potential at a constant pH of 8 over the sampling days, showing an increase from -2.5 to 0 mV as the geometric mean size of MNBs coarsens from 600 nm to 2-3 μm . The bubbles predominantly exhibited a negative surface charge, consistent with the literature (Ulatowski et al., 2019; Bui et al., 2019). The zeta potential enhancement intensifies surface repulsion forces, preventing bubble coalescence (Elmahdy et al., 2008). The surface charge of MNBs is positively correlated with pH, and the addition of chemical agents like MIBC can reduce MNB size and zeta potential (Ahmadi et al., 2014; Pourkarimi et al., 2021).

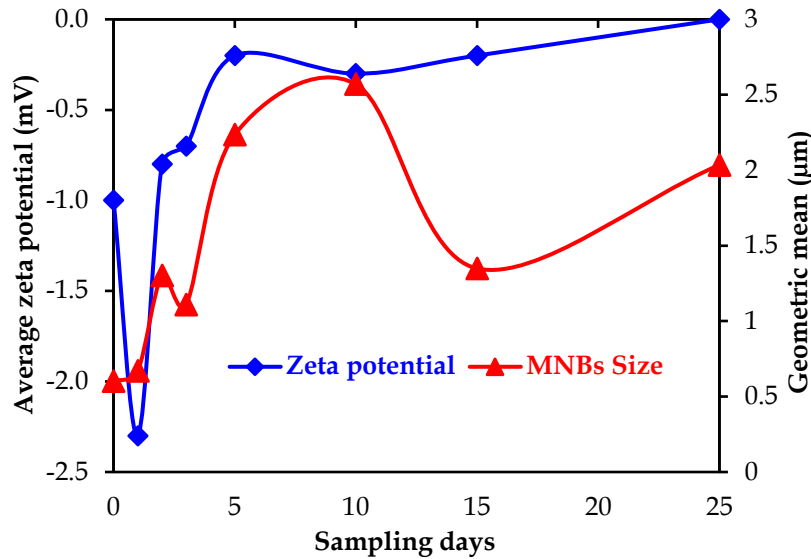


Fig. 6. Correlation between size variations and zeta potential fluctuations of micro-nanobubbles over distinct sampling days (The laboratory conditions included distilled water, a pH of 8, free of chemical reagents, and were conducted at room temperature of $25\pm 2^\circ\text{C}$)

3.2. Effect of ultrasonic treatment

Fig. 7 displays the backscattered FESEM images and EDS results (Map Sum Spectrum) of pure pyrite particles with a size fraction of $(-105+53 \mu\text{m})$ before and after undergoing treatment with ultrasonic waves, respectively. Fig. 7b shows that before the ultrasonic treatment of pyrite particles, a coating of particles $(-335.4+20.38 \mu\text{m})$ surrounds the surface of the pyrite particles. Fig. 7d illustrates a significant reduction in the number of ultra-fine particles and the cleaning of the surface of the pyrite particles after 5 min of treatment with ultrasonic waves (at 80% power and 37 kHz frequency). Overall, as clearly indicated in Fig. 8, ultrasonic waves have a positive effect on the weight distribution of elements on the surface of the pyrite particles. The increase in the weight percentage of sulfur (by 2.8% wt.% S) and iron (by 3.02 wt.% Fe), along with the reduction in the weight percentage of oxygen (by 5.82% wt.% O), can lead to an improvement in the physical and chemical properties of these particles.

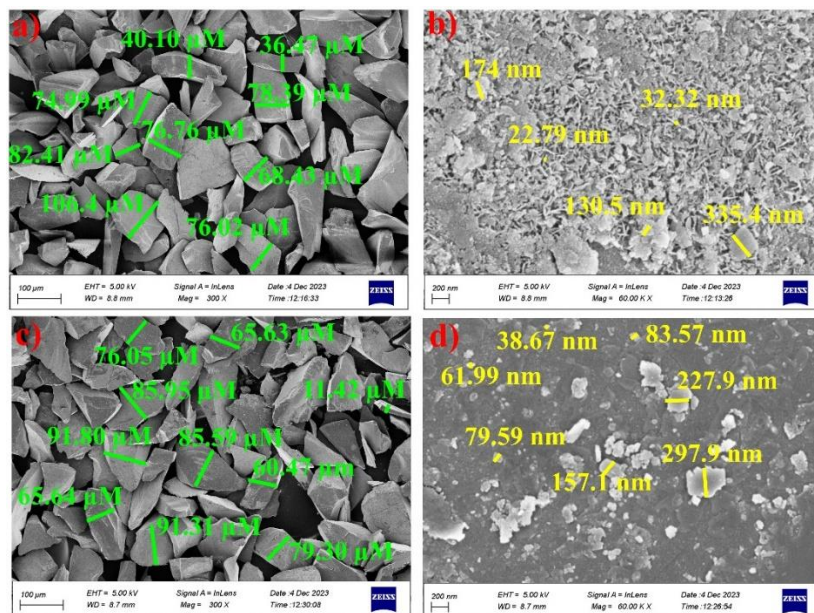


Fig. 7. Secondary electron FESEM images of pyrite particles before (top) and after (bottom) ultrasonic treatment at scales of $100 \mu\text{m}$ and 200nm (The laboratory conditions involved pure pyrite mineral particles $(-105+53 \mu\text{m})$, exposed to ultrasonic waves for 5 min at 80% power and a frequency of 37 kHz, conducted at room temperature)

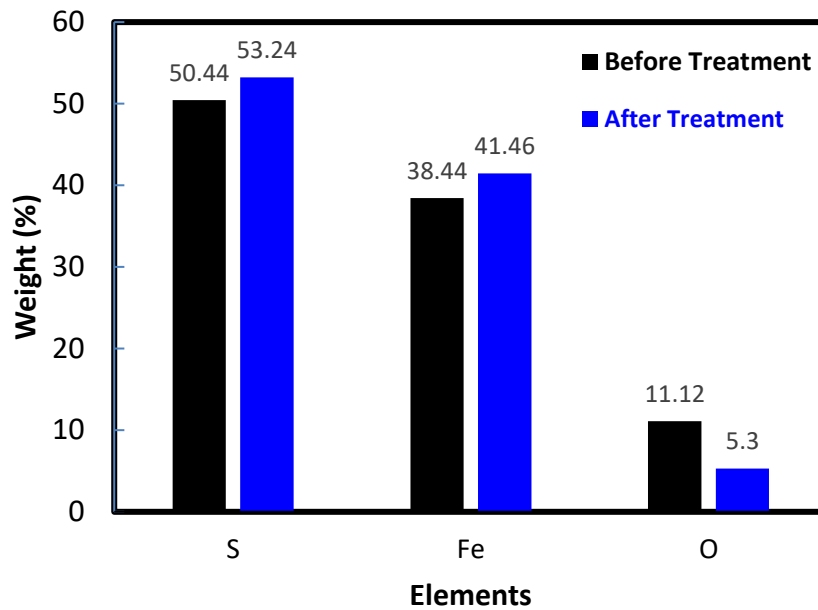


Fig. 8. Comparison of element distribution on the surface of pyrite particles (-105+53 μm) before and after treatment with ultrasonic waves

3.3. Effect of micro-nanobubbles on pyrite flotation in the absence and presence of SIPX

Fig. 9 illustrates the flotation recovery of a high-purity pyrite sample as a function of (a) pH and (b) SIPX dosage with and without MNBs. The results show higher iron recovery with MNBs across pH 8-11 and SIPX dosage (i.e., 0-175 μM). The optimal pH of 9 was chosen, resulting in an 11% increase in iron recovery in the presence of MNBs as shown in Fig. 9a. The recovery of pyrite (with and without MNBs) reduced with increasing pH, regardless of the collector concentration. One reason for the reduced recovery of the pyrite in alkaline environments and its poor attachment to air bubbles can be attributed to the gradual deposition of hydrophilic-oxidation products ($\text{Fe}(\text{OH})_3$, SO_4^{2-} , etc.) on the surface of pyrite (Jiang et al., 2023).

Contrary to pH, the impact of SIPX dosage (i.e., 0-175 μM) with and without MNBs on pyrite recovery was observed to vary (Fig. 9b). In the absence of MNBs, the highest pyrite recovery reached was 16% at a collector concentration of 50 μM , while with MNBs, the recovery increased to 30%. The decrease in collector consumption in the presence of MNBs can be linked to several factors including heightened hydrophobic attraction, diminished electrostatic repulsion, improved macroscopic contact angle between particles and bubbles (Ma and Tao, 2022), selective adsorption, and the formation of a nanobubble layer on the particle surface (Tao, 2022). As indicated in previous research works, this phenomenon may have occurred through the hydrophobic interaction between micro-nano bubbles and the pyrite surface, where the presence of MNBs appears to have acted as secondary collectors, enhancing the contact surface of pyrite particles with coarse bubbles (Azevedo et al., 2016).

3.4. Effect of micro-nanobubbles on absorption capacity

Studying the absorption of the SIPX collector on pyrite surfaces, with and without micro-nano bubbles is essential for enhancing pyrite flotation efficiency and understanding sulfide mineral floatability. To investigate this, changes in the absorbance intensity of the SIPX collector solution were measured using a spectrometer. Fig. 10 illustrates the absorption test of the SIPX collector on the adsorbent (pure pyrite mineral) at concentrations of 80 and 160 μM with and without MNBs.

The UV spectrophotometer measured xanthate concentration in the 200-400 nm range showing distinguishable peaks at 228 and 301 nm with an absorption ratio of approximately 1:2. The peak at $\lambda=301$ nm is identified as the most suitable absorption peak for the SIPX collector, as it minimize errors from nonlinearity. This wavelength selection aligns with findings from previous studies (Agorhom et al., 2014; Han et al., 2020; Heidari et al., 2024).

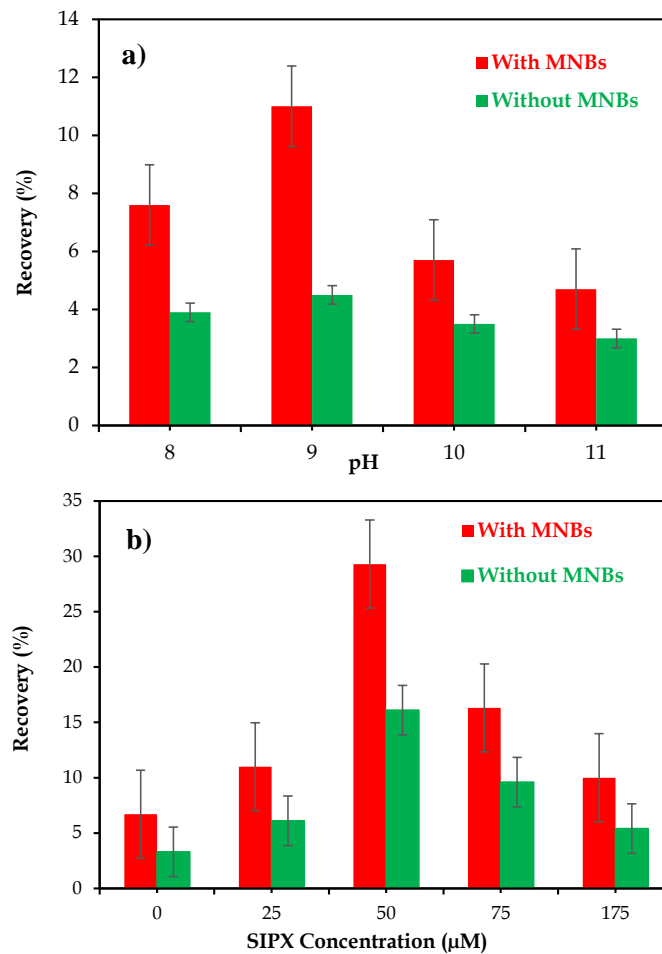


Fig. 9. Variation in pyrite recovery based on (a) pH and (b) SIPX collector concentration (The laboratory conditions included distilled water, pure pyrite mineral (particle size distribution: 53 to 105 μm), sodium isopropyl xanthate (SIPX) collector (concentrations: 0 to 175 μM), a pH of 8 to 11, a room temperature of $25\pm 2^\circ\text{C}$, and each condition was repeated three times)

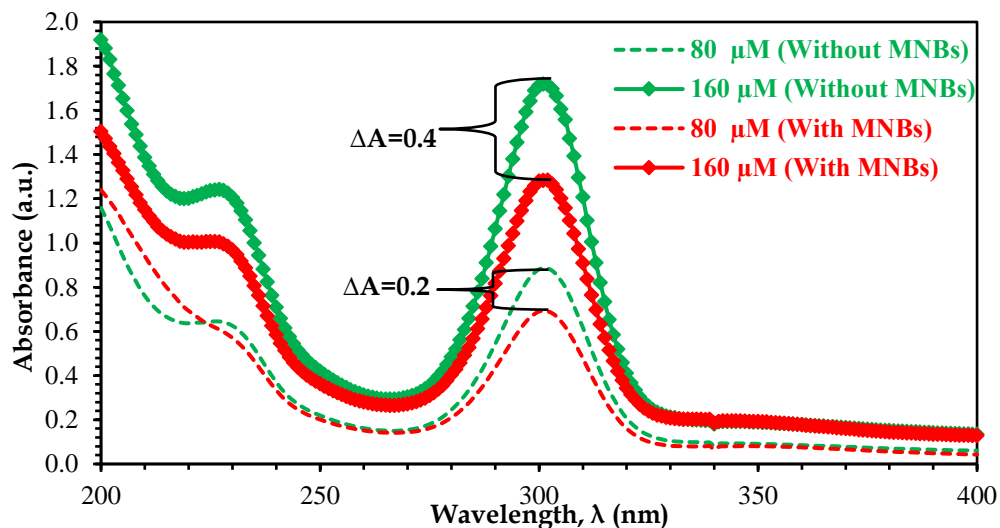


Fig. 10. UV-Vis spectra of the aqueous solution of the SIPX collector with and without MNBs after 20 min contact with the adsorbent (pyrite) (The laboratory conditions included pure pyrite mineral particles ($-105+53 \mu\text{m}$) in a SIPX collector solution, both with and without MNBs, at collector concentrations of 80 and 160 μM , a pH of 9, a temperature of $25\pm 2^\circ\text{C}$, and each condition was repeated three times)

The data presented in Fig. 10 depicts the variations in SIPX collector absorption intensity on the adsorbent (pyrite) with and without micro-nano bubbles after filtration. The results indicate a 0.4% reduction in absorption intensity at a high SIPX concentration (160 μM) in the presence of micro-nanobubbles compared to their absence and a 0.2% reduction at a low SIPX concentration (80 μM). Each experiment was conducted in triplicate, and the experimental error was assessed at a 95% confidence level. The difference in absorption intensity measured using the UV method can serve as evidence for the presence of stable micro-nanobubbles in the suspension and their impact on the pyrite surfaces and even the collector. These changes in absorbance intensity can serve as evidence for the presence of stable micro-nanobubbles in the suspension and their impact on the surfaces of pyrite as well as the collector. Generally, it is observed that stable micro-nanobubbles contribute to the increased adsorption of the SIPX collector on the pyrite surface. The presence of MNBs may lead to increased contact area and improved distribution of the collector in the suspension, resulting in enhanced adsorption. Therefore, although a slight reduction in absorbance intensity has been observed, these results indicate the positive effect of MNBs on the SIPX adsorption process on pyrite.

Fig. 11 illustrates the relationship between collector concentration and SIPX adsorption capacity in the presence and absence of MNBs. The findings indicate that the adsorption capacity of SIPX increases as the collector concentration arises, regardless of the presence of MNBs.

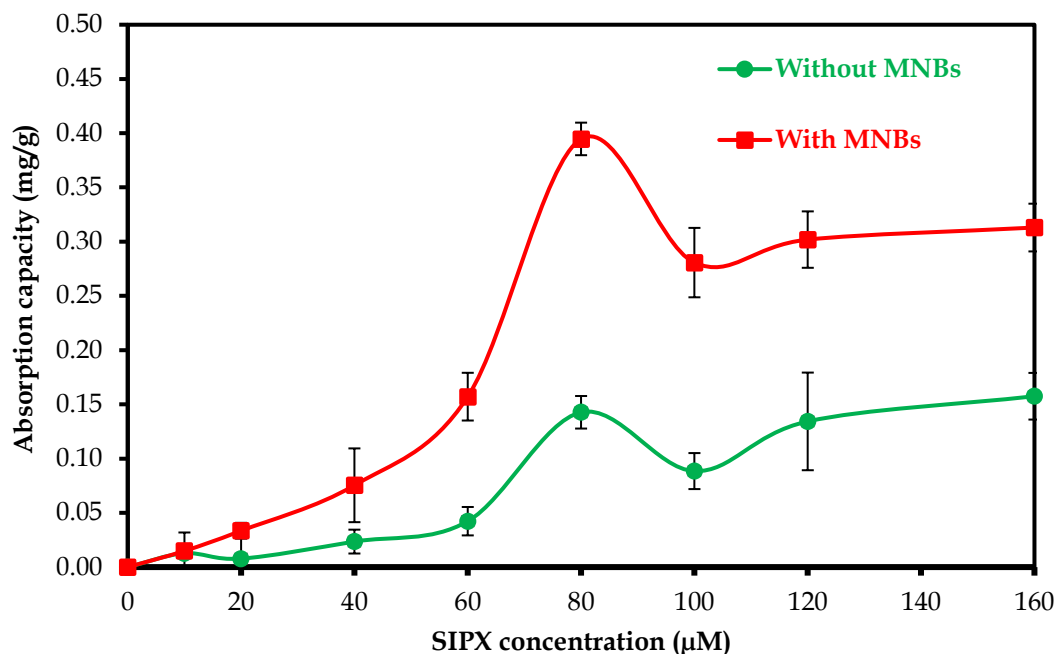


Fig. 11. Adsorption curves of pyrite with respect to the SIPX collector concentration (The laboratory conditions included pure pyrite mineral particles (-105+53 μm) in a SIPX collector solution, both with and without MNBs, at collector concentrations of 80 and 160 μM , a pH of 9, a temperature of $25\pm 2^\circ\text{C}$, and each condition was repeated four times)

According to the results presented, the adsorption capacity of SIPX increases as the collector concentration rises in both scenarios, with and without MNBs. Based on the findings depicted in Fig. 11, in the absence of micro-nanobubbles, the uptake capacity increases gradually from 0.01 to 0.04 mg/g with a gentle slope as the SIPX collector concentration rises from 10 to 60 μM . Subsequently, with an increase in collector concentration up to 80 μM , the sorption trend escalates to 0.14 mg/g with a steeper slope. However, beyond this point, as the collector concentration reaches 100 μM , the sorption trend reverses and decreases to 0.08 mg/g. On the contrary, in the presence of micro-nanobubbles, a notable increase in the adsorption capacity from 0.01 mg/g to 0.39 mg/g is observed as the collector concentration enhances from 10 to 80 μM . Furthermore, with a further increase in collector concentration up to 100 μM , the sorption capacity decreases to 0.28 mg/g. Nevertheless, the results indicate that overall, the pyrite sorption level in the presence of micro-nanobubbles surpasses that in their absence

across the entire collector concentration range. The adsorption capacity of the SIPX collector on pyrite significantly increased to 1.6 times in the presence of micro-nanobubbles compared to their absence.

3.5. Effect of MNBs on the bulk flotation

Fig. 12 illustrates the relationship between flotation time and iron recovery from gold-bearing copper ore in the presence and absence of micro-nanobubbles. Iron recovery significantly increased during the first 2 min of flotation time, both with and without micro-nanobubbles. Under these conditions, the highest iron recovery occurred in the presence of micro-nanobubbles. However, after 20 min of flotation, the final iron recovery significantly increased from 18.5% to 32.5% in the presence of micro-nanobubbles. The higher final recovery is likely due to the presence of micro-nanobubbles on the surface of pyrite particles (a relatively hydrophobic mineral) and the increased attachment force of larger bubbles to the hydrophobic particles (Azevedo et al., 2016). Furthermore, the significant loss of iron values in the absence of micro-nanobubbles may be associated with the oxidation of pyrite surfaces (Wu et al., 2023).

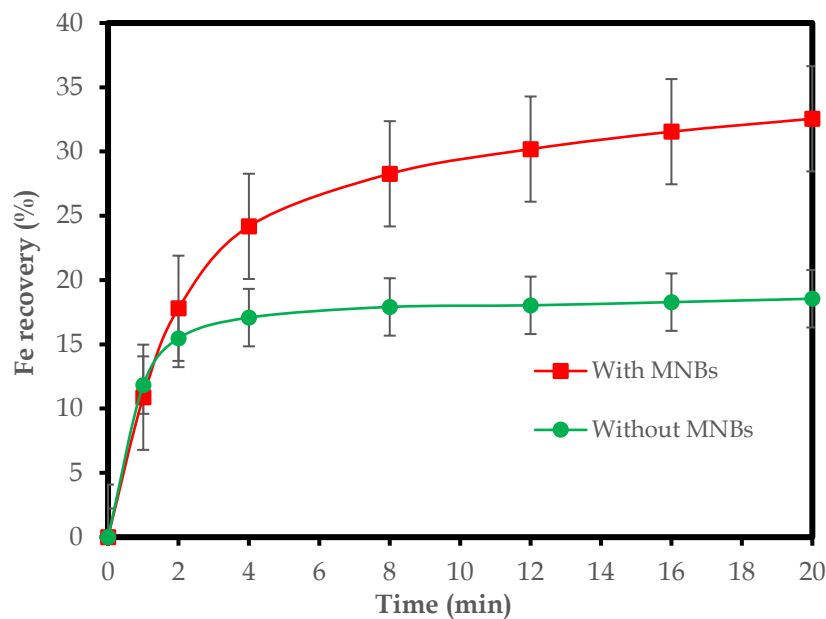


Fig. 12. Recovery of iron as a function of flotation time with and without micro-nano bubbles (The experimental conditions were a 2.5-liter Denver flotation cell, stirring speed of 900 rpm, solid ratio of 30%, sodium isopropyl xanthate (40 g/Mg), methyl isobutyl carbinol (90 g/Mg), pH 9, with three repetitions)

As shown in Fig. 13, the iron grade in the concentrate was enriched to 26% and 24.5%, respectively, with and without micro-nano bubbles, while the iron content in the final tailings remained relatively unchanged at 3.3% and 3%. Previous studies indicated that the improvement in grade and recovery during flotation with micro-nanobubbles can be attributed to several key factors. Specifically, micro-nanobubbles exhibit a high surface area to volume ratio, promoting enhanced interaction with hydrophobic particles during the flotation process, thereby improving attachment and flotation efficiency (Kyzas et al., 2021; Ma and Tao, 2022; Cheng et al., 2023). Additionally, nanobubbles enhance gas hold-up in flotation cells and lead to an improvement in flotation efficiency (Pourkarimi et al., 2018). Furthermore, the presence of bulk microbubbles (BMBs) and bulk nanobubbles (BNBs) substantially enhances particle recovery through the bridging mechanism, thereby reinforcing the attachment of conventional bubbles to particles (Azevedo et al., 2016; Zhou et al., 2022). Moreover, following the formation of a layer or cluster of MNBs on hydrophobic surfaces, the extremely small bubbles promote the adherence of particles to regular bubbles at specific or selective sites, significantly increasing the particle-bubble contact angle compared to the absence of MNBs (Calgaroto et al., 2016; Tao et al., 2021).

The flotation rate constants determined using the classical first-order flotation kinetic model were found to be 0.4 min^{-1} and 1 min^{-1} in the presence and absence of MNBs, individually. The corresponding standard deviations at a 95% confidence level were 1.5% and 0.4%, respectively.

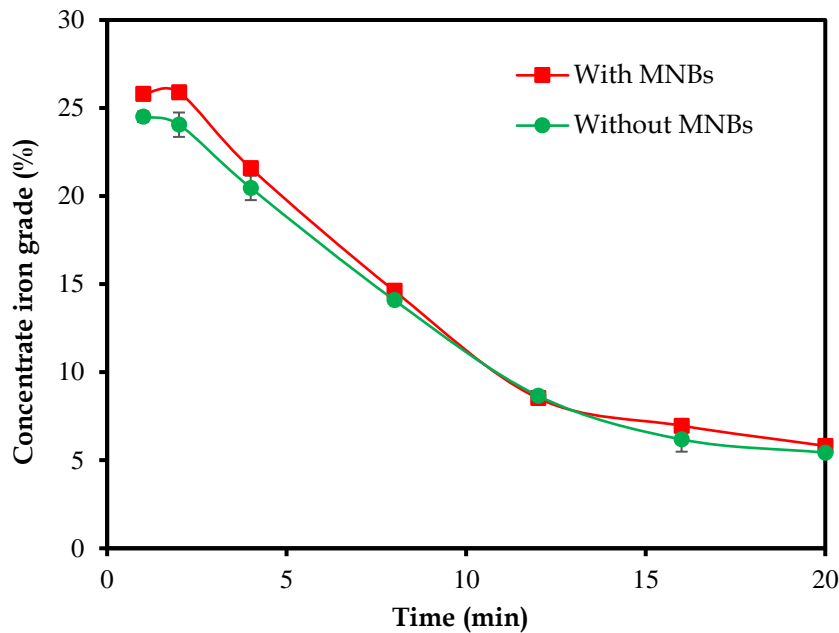


Fig. 13. Relationship between an iron grade in the concentrate and the flotation time with and without micro-nanobubbles (number of repeats= 3)

3.6. The kinetics of adsorption

Studying the kinetics of the process and how it is affected is a crucial element in assessing the effectiveness of adsorption systems. It plays a pivotal role in the design of sorption operations. Therefore, an investigation into process kinetics was conducted to provide a more comprehensive description of the sorption process and to enhance our understanding of the sorption mechanism. In this study, 0.5 g of pure pyrite mineral with particle sizes ranging from 53 to 105 μm were mixed in water containing sodium isopropyl xanthate (SIPX) collector, both in the presence and absence of micro-nanobubbles (MNBs) at room temperature (25°C) for 20 min.

Fig. 14 illustrates the adsorption capacity as a function of contact time between the pyrite surface and the SIPX collector. The results show that the adsorption capacity increases with longer contact times. Specifically, in the absence of MNBs, the sorption capacity rises rapidly from 0 to 0.9 mg/g within the first 2 min and then stabilizes around 0.19 mg/g. Conversely, in the presence of MNBs, this increase is more pronounced, with the uptake capacity escalating from 0 to 0.29 mg/g in the first 2 min, followed by a steady increase to 0.377 mg/g over the entire 20-min period. The error bars indicate a relatively low standard deviation, suggesting the reliability of the data. This disparity highlights the significant impact of micro-nanobubbles in enhancing sorption capacity, thereby improving the efficiency of the adsorption process.

Additionally, the sorption kinetics of SIPX on the pyrite surface were evaluated using three established and commonly employed kinetic models: the pseudo 1st order, pseudo 2nd order, and intra-particle diffusion models, as depicted in Figs. 15 and 16 [49-52]. The pseudo-first-order (PFO) and pseudo-second-order (PSO) models are categorized as adsorption reaction models, while the intra-particle diffusion model represents an adsorption diffusion mechanism (Amrollahi et al., 2019). Generally, the PFO kinetic model depicts that the efficiency of sorption is relative to the number of empty sites, while PSO kinetics illustrates that the chemical sorption is a rate-limiting step and controls the sorption operations (Ghiasi et al., 2020). The intra-particle diffusion model is commonly utilized to interpret experimental data used to identify the mechanisms of pore diffusion involved in sorption processes (Chen and Zeng, 2017). The mathematical formulations for these models, which are utilized

to estimate the kinetic parameters, are provided in Table 3 (Ávila-Márquez et al., 1963; Amrollahi et al., 2019; Forghani et al., 2020).

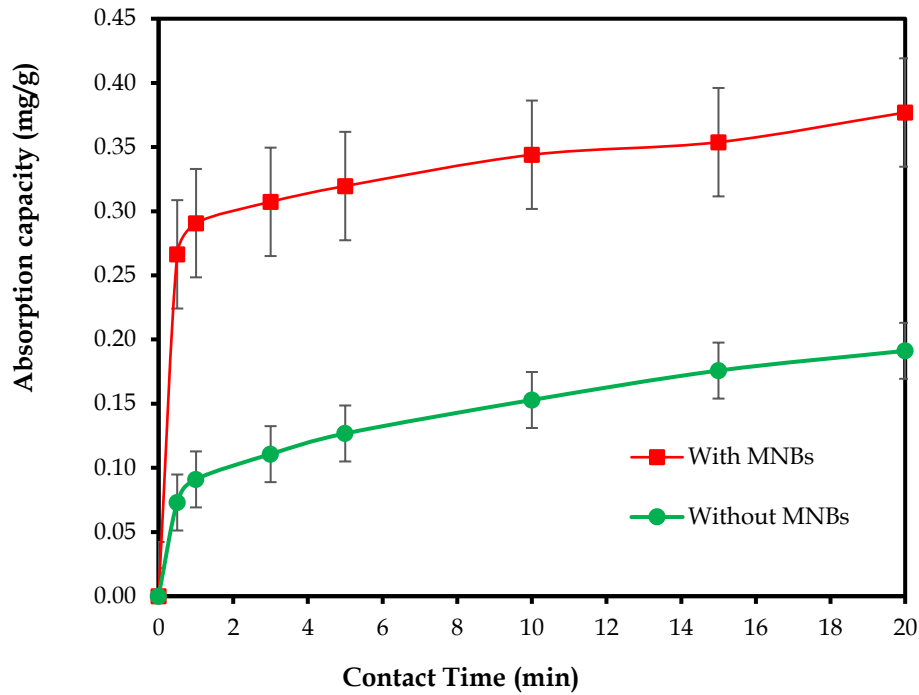


Fig. 14. Adsorption capacity of SIPX collector as a function of contact time (The experimental conditions were a collector concentration of 60 μM , pH of 9, temperature of $25\pm 2^\circ\text{C}$, and number of repeats equal to 3)

Table 3. Different models are employed to characterize the kinetic behavior of a pure pyrite sample

Equation	Model	Equation number
$\ln(q_e - q_t) = \ln q_e - k_1 t$	Pseudo 1 st order model	(2)
$q_t = \frac{q_e^2 k_2 t}{1 + k_2 q_e t}$	Pseudo 2 nd order model	(3)
$q_t = k_{ipd} t^{0.5} + C$	Intra-particle diffusion model	(4)

where, q_e and q_t (mg/g) represent the quantities of collector adsorbed at equilibrium and time t , respectively. Meanwhile, k_1 (1/min), k_2 (g/mg.min), and k_{ipd} (mg. g/min^{0.5}) denote the specific adsorption rate constants for the pseudo first order, pseudo second order, and intra-particle diffusion models, respectively. Additionally, C stands for the intercept.

Figs. 15 and 16 depict the fitting of the experimental data to the adsorption reaction (pseudo 1st order and pseudo 2nd order) and (intra-particle) diffusion models. The estimated kinetic parameters are also detailed in Table 4.

By examining the magnitudes of R^2 for each model in the presence ($R^2 = 0.9774$) and absence ($R^2 = 0.9238$) of MNBs, it is evident that the pseudo 2nd order model exhibits the best fit with the kinetic data, suggesting that the sorption of SIPX onto pyrite entails a chemical adsorption mechanism. Additionally, the model proposed by Weber and Morris (1963) (Eq. 4) was employed to forecast the rate-controlling step in the sorption process, as depicted in Fig. 16 and Table 4. The findings validated a two-stage sorption process (Fig. 16), indicating that SIPX adsorption was not solely governed by intra-particle diffusion. Based on the data presented in Fig. 16, the initial segment exhibits a sharp incline, suggesting the rapid migration of SIPX ions from the solution to the outer surface of the pyrite particles in the presence of MNBs. This steep ascent in the first phase is attributed to external surface adsorption. Conversely, the subsequent segment reflects the diminished concentration of SIPX remaining in the solution, leading to a gradual intra-particle diffusion within the pores.

Table 4. Kinetic parameters for the adsorption of SIPX on pyrite at an initial concentration of 60 μM

		Model	Kinetic parameters	
Without MNBs	Pseudo 1 st order		k_1 (min^{-1})	0.654
			$q_{e,cal}$ (mg g^{-1})	0.161
			R^2	0.8370
	Pseudo 2 nd order		k_2 ($\text{g mg}^{-1} \text{min}^{-1}$)	4.758
			$q_{e,cal}$ (mg g^{-1})	0.179
			R^2	0.9238
	Intra-particle diffusion		$k_{ip,1}$ ($\text{mg g}/\text{min}^{0.5}$)	0.034
			C_1	0.051
			R^2	0.9077
			$k_{ip,2}$ ($\text{mg g}/\text{min}^{0.5}$)	0.029
			C_2	0.060
			R^2	0.9988
Pseudo 1 st order		k_1 (min^{-1})	2.77	
		$q_{e,cal}$ (mg g^{-1})	0.337	
		R^2	0.9541	
Pseudo 2 nd order		k_2 ($\text{g mg}^{-1} \text{min}^{-1}$)	15.18	
		$q_{e,cal}$ (mg g^{-1})	0.351	
		R^2	0.9774	
Intra-particle diffusion		$k_{ip,1}$ ($\text{mg g}/\text{min}^{0.5}$)	0.036	
		C_1	0.246	
		R^2	0.7638	
		$k_{ip,2}$ ($\text{mg g}/\text{min}^{0.5}$)	0.024	
		C_2	0.265	
		R^2	0.9615	

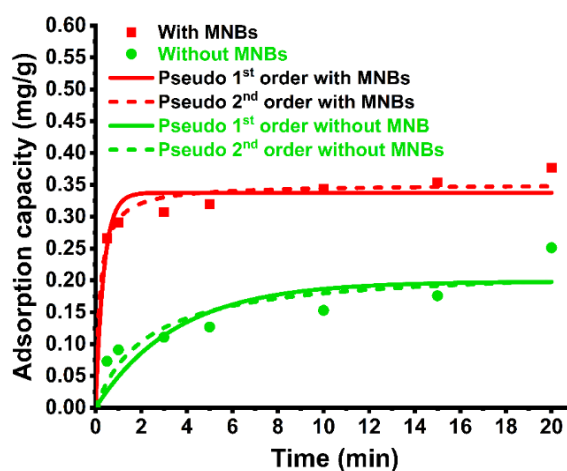


Fig. 15. Comparison of pseudo-first-order and pseudo-second-order kinetic models for SIPX adsorption onto pyrite with and without the presence of MNBs (Conditions: collector concentration of 60 μM , contact time of 0 to 20 min, and room temperature of $25\pm 2^\circ\text{C}$)

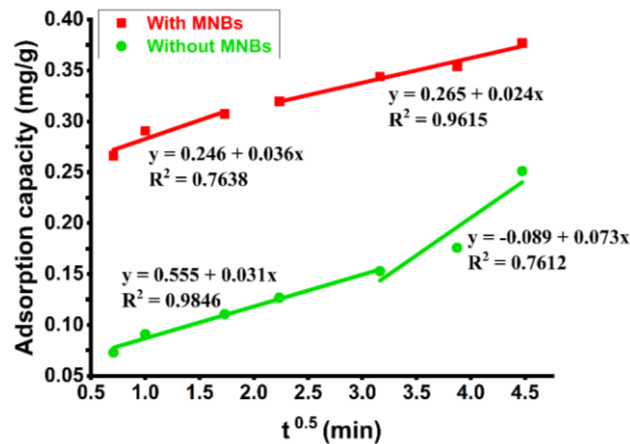


Fig. 16. Intra-particle diffusion analysis of SIPX adsorption onto pyrite with and without the presence of MNBs (Conditions: collector concentration of 60 μ M, contact time of 0 to 20 min, and room temperature of $25\pm 2^\circ\text{C}$)

4. Conclusions

The research examined the floatability of pyrite mono-mineral and pyrite-containing copper ore with and without micro-nano bubbles (MNBs), analyzing their adsorption properties and kinetics. Results indicated that MNBs enhanced the iron flotation process for both pyrite mono-mineral and pyrite-bearing ore. At pH 9, pyrite recovery increased by 30% with the presence of micro-nanobubbles (MNBs). Ultrasonic treatment of pyrite particles compared to untreated ones resulted in a reduction of ultrafine surface coatings, increased purity (higher S, Fe content), and decreased surface oxidation (lower O content), indicating an enhancement in liberation and mineral quality. A comparison of recovery in micro-flotation experiments at pH 9 with varying SIPX collector concentrations revealed a considerable difference when micro-nano bubbles were introduced. Flotation tests on pyrite-bearing copper ore showed a 0.8% increase in ultimate grade and an 8% rise in recovery with micro-nano bubbles. Analysis of the flotation rate constant indicated that the micro-nano bubbles followed the first-order kinetic model. The study examined the adsorption of the SIPX collector on pure pyrite with and without MNBs at a wavelength of 301 nm using a UV spectrometer, confirming the superior performance of MNBs during the flotation process. The study on the adsorption impact of SIPX dosage and contact time revealed that the presence of MNBs resulted in a 1.6-fold enhancement in the uptake capacity compared to the absence of MNBs. The sorption mechanism was examined using various kinetic models (pseudo 1st, pseudo 2nd order, and intra-particle diffusion), and it was found that in the presence of MNBs, adsorption intensity increased, and the dominant mechanism was chemical. Indeed, the introduction of micro-nanobubbles as an active agent facilitated an enhancement in the chemical adsorption of the collector on the pyrite surface.

Acknowledgments

This work is based upon research funded by Iran National Science Foundation (INSF) under project No.4021600. The authors are grateful for the financial support provided by the INSF. We are also genuinely thankful to the Qale-Zari Copper Mine staff for providing samples and supporting this research study. We sincerely appreciate Dr. Mohammad Hasanzadeh (Pharmaceutical Analysis Research Center, Tabriz University of Medical Sciences) for his valuable insights and ongoing support. The first author also expresses utmost gratitude and appreciation to Ms. Soheila Hassanzadeh for her collaboration and assistance in conducting the adsorption tests.

Appendix A

Plotting the remaining material in the cell against time on a semi-logarithmic scale revealed a linear relationship with a slope (k) representing first-order kinetics for both scenarios with and without micro-nano bubbles (MNBs). This observation is illustrated in Fig. A1.

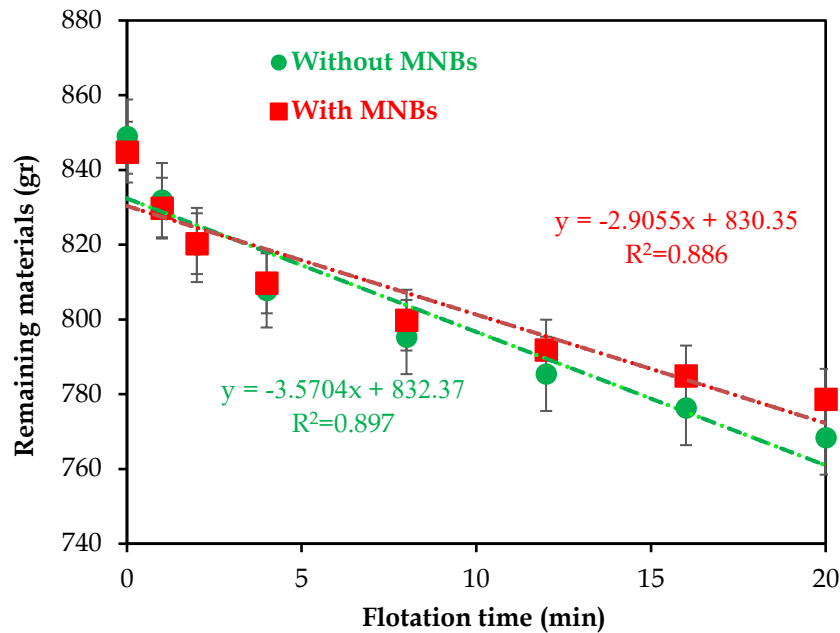


Fig. A1. Material remaining in the cell over flotation duration (The experimental conditions were a 2.5-dm³ Denver flotation cell, stirring speed of 900 rpm, solid ratio of 30%, sodium isopropyl xanthate (40 g/Mg), methyl isobutyl carbinol (90 g/Mg), pH 9, with three repetitions)

References

- AGORHOM, E.A., SKINNER, M., ZANIN, M., 2014. *Diethylenetriamine depression of Cu-activated pyrite hydrophobised by xanthate*. *Miner. Eng.* 57, 36-42.
- AHMADI, R., KHODADADI, D.A., ABDOLLAHY, M., FAN, M., 2014. *Nano-microbubble flotation of fine and ultrafine chalcopyrite particles*. *Int. J. Min. Sci. Technol.* 24, 559-566.
- ALLARD, O., LOPEZ, M., DEMERS, I., COUDERT, L., 2022. *Gold recovery from sulfide concentrates produced by environmental desulfurization of mine tailings*. *Minerals* 12, 1011.
- ALTUN, N.E., GÜLER, T., AKDEMİR, Ü., 2010. *Pyrite flotation—a review*. In *Proceedings of the XIIth International Mineral Processing Symposium, Cappadocia-Nevşehir, Turkey, 6-8 October*, 295-303.
- AMROLLAHI, A., MASSINAEI, M., MOGHADDAM, A.Z., 2019. *Removal of the residual xanthate from flotation plant tailings using bentonite modified by magnetic nano-particles*. *Miner. Eng.* 134, 142-55.
- AVILA-MARQUEZ, D.M., BLANCO-FLORES, A., REYES-DOMINGUEZ, I.A., TOLEDO-JALDIN, H.P., AGUILAR-CARRILLO, J., CRUZ-GAONA, R., 2020. *Copper sulfide flotation under acidic conditions using a xanthogen formate compound as collector: Adsorption studies and experimental design approach*. *Colloids Surf. A: Physicochem. Eng. Asp.* 585, 124032.
- AZEVEDO, A., ETCHEPARE, R., CALGAROTO, S., RUBIO, J., 2016. *Aqueous dispersions of nanobubbles: Generation, properties and features*. *Miner. Eng.* 94, 29-37.
- BILAL, M., PARK, I., HORNN, V., HASSAN, F.U., JEON, S., HIROYOSHI, N., 2022. *The challenges and prospects of recovering fine copper sulfides from tailings using different flotation techniques: A review*. *Minerals* 12, 586.
- BUI, T.T., NGUYEN, D.C., HAN, M., 2019. *Average size and zeta potential of nanobubbles in different reagent solutions*. *J. Nanopart. Res.* 21, 73.
- CAO, M., LIU, Q., 2006. *Reexamining the functions of zinc sulfate as a selective depressant in differential sulfide flotation-The role of coagulation*. *J. Colloid. Interface. Sci.* 301, 523-531.
- CALGAROTO, S., AZEVEDO, A., RUBIO, J., 2016. *Separation of amine-insoluble species by flotation with nano and microbubbles*. *Miner. Eng.* 89, 24-29.
- CHENG, G., ZHANG, M.N., LI, Y.L., LAU, E.V., 2023. *Improving micro-fine mineral flotation via micro/nano technologies*. *Sep. Sci. Technol.* 58, 520-537.
- CHEN, B., ZENG, B., 2017. *Characteristics of micro-interface adsorption kinetics between sediments and Cu ions*. *Int. J. Sediment Res.* 32(1), 82-89.

- DENG, Z., CHENG, W., TANG, Y., TONG, X., LIU, Z., 2021. *Adsorption mechanism of copper xanthate on pyrite surfaces*. Physicochemical Problems of Mineral Processing. 57, 46-60.
- DUNNE, R., 2005. *Flotation of gold and gold-bearing ores. Chapter 14, Developments in mineral processing*. Eds. ADAMS, M.D., WILS, B.A. Elsevier, 15, 309-44.
- ELMAHDY, A.M., MIRNEZAMI, M., FINCH, J.A., 2008. *Zeta potential of air bubbles in presence of frothers*. Int. J. Miner. Process. 89, 40-43.
- FENG, Q., YANG, S., WEN, S., WANG, H., ZHAO, W., HAN, G., 2022. *Flotation of copper oxide minerals: A review*. Int. J. Min. Sci. Technol. 32, 1351-1364.
- FORGHANI, M., AZIZI, A., LIVANI, M.J., KAFSHGARI, L.A., 2020. *Adsorption of lead (II) and chromium (VI) from aqueous environment onto metal-organic framework MIL-100 (Fe): Synthesis, kinetics, equilibrium and thermodynamics*. J. Solid State Chem. 291,121636.
- FORREST, K., YAN, D., DUNNE, R., 2001. *Optimisation of gold recovery by selective gold flotation for copper-gold-pyrite ores*. Miner. Eng. 14, 227-241.
- GHIASI, E., MALEKZADEH, A., 2020. *Removal of various textile dyes using LaMn(Fe)O₃ and LaFeMn_{0.5}O₃ nanoperovskites; RSM optimization, isotherms and kinetics studies*. J. Inorg. Organomet. Polym. 30, 2789-2804.
- GU, G.H., SUN, X.J., LI, J.H., HU, Y.H., 2010. *Influences of collector DLZ on chalcopyrite and pyrite flotation*. J. Cent. South Univ. 17, 285-288.
- HAN, C., WEI, D., GAO, S., ZAI, Q., SHEN, W., 2020. *Adsorption and desorption of butyl xanthate on chalcopyrite*. J. Mater. Res. Technol. 9, 12654-60.
- HEIDARI, H., AZIZI, A., HASSANZADEH, A., 2024. *A New insight into the mechanism of MNB-assisted flotation of copper: A link between chalcopyrite and its-bearing bulk ore*. Mineral Engineering. 216, 108882.
- HASSANZADEH, A., GHOLAMI, H., ÖZKAN, S.G., NIEDOBA, T., SUROWIAK, A., 2021. *Effect of power ultrasound on wettability and collector-less floatability of chalcopyrite, pyrite and quartz*. Minerals 11, 48.
- HASSANZADEH, A., HASANZADEH, M., 2016. *A study on selective flotation in low and high pyritic copper sulphide ores*. Sep. Sci. Technol. 51, 2214-2224.
- HASSANZADEH, A., KARAKAS, F., 2017. *The kinetics modeling of chalcopyrite and pyrite, and the contribution of particle size and sodium metabisulfite to the flotation of copper complex ores*. Part. Sci. Technol. 15, 455-61.
- HE, H., XIAN, H., ZHU, J., TAN, W., WU, X., YANG, Y., LI, S., QIU, K., ZHU, R., HENRY TENG, H., 2023. *Evaluating the physicochemical conditions for gold occurrences in pyrite*. Am. Min. 108, 211-216.
- JIANG, K., HAN, Y., LIU, J., WANG, Y., GE, W., ZHANG, D., 2023. *Experimental and theoretical study of the effect of pH level on the surface properties and floatability of pyrite*. Appl. Surf. Sci. 615, 156350.
- KHOSHDAST, H., HASSANZADEH, A., KOWALCZUK, P.B., FARROKHPAY, S., 2023. *Characterization techniques of flotation frothers-A review*. Miner. Process. Extr. Metall. Rev. 44, 77-101.
- KRUSZELNICKI, M., HASSANZADEH, A., LEGAWIEC, K.J., POLOWCZYK, I., KOWALCZUK, P.B., 2022. *Effect of ultrasound pre-treatment on carbonaceous copper-bearing shale flotation*. Ultrason. Sonochem. 84, 105962.
- KYZAS, G.Z., MITROPOULOS, A.C., MATIS, K.A., 2021. *From microbubbles to nanobubbles: Effect on flotation*. Processes 9, 1287.
- MA, F., TAO, D., 2022. *A study of mechanisms of nanobubble-enhanced flotation of graphite*. Nanomaterials 12, 3361.
- NAZARI, S., ZHOU, A., HASSANZADEH, A., LI, J., HE, Y., BU, X., KOWALCZUK, P.B., 2022. *Influence of operating parameters on nanobubble-assisted flotation of graphite*. J. Mater. Res. Technol. 20, 3891-3904.
- NAZARI, S., HASSANZADEH, A., 2020. *The effect of reagent type on generating bulk sub-micron (nano) bubbles and flotation kinetics of coarse-sized quartz particles*. Powder Technol. 374, 160-171.
- NAZARI, S., HASSANZADEH, A., KOSHDAST, H., KOWALCZUK, P.B., 2022. *Recent developments in generation, detection and application of nanobubbles in flotation*. Minerals 12, 462.
- NIKOU EI MAHANI, A., KARAMOOZIAN, M., JAHANI CHEGENI, M., MAHMOODI MEYMAND, M., 2024. *Effect of stable nano-microbubbles on sulfide copper flotation and reduction of chemicals dosage*. JME 15, 261-283.
- OLSZOK, V., RIVAS-BOTERO, J., WOLLMANN, A., BENKER, B., WEBER, A.P., 2020. *Particle-induced nanobubble generation for material-selective nanoparticle flotation*. Colloids Surf. A: Physicochem. Eng. Asp. 592, 124576.
- OTSUKI, A., ZHAO, Y., 2018. *UV-Vis Study of mixed collector adsorption on pyrite towards the better understanding of the adsorption mechanism*. Curr. Work. Miner. Process. 1, 13-20.
- OZUN, S., HASSAS, B.V., MILLER, J.D., 2019. *Collectorless flotation of oxidized pyrite*. Colloids Surf. A: Physicochem. Eng. Asp. 561, 349-356.

- PANAYOTOV, V., PANAYOTOVA M., 2023. *Technology for increasing the precious metals content in copper concentrate obtained by flotation*. Physicochem. Probl. Miner. Process. 59.
- POURKARIMI, B., REZAI, M., NOPARAST, A.V., NGUYEN, S.C., 2021. *Proving the existence of nanobubbles produced by hydrodynamic cavitation and their significant effects in powder flotation*. Adv. Powder Technol. 32, 1810-1818.
- POURKARIMI, Z., REZAI, B., NOAPARAST, M., 2018. *Nano bubbles effect on the mechanical flotation of phosphate ore fine particles*. Physicochem. Probl. Miner. Process. 54, 278-292.
- QIN, H., GUO, X.Y., TIAN, Q.H., ZHANG, L., 2021. *Recovery of gold from refractory gold ores: Effect of pyrite on the stability of the thiourea leaching system*. Int. J. Miner. Metall. Mater. 28, 956-964.
- SHADMAN, M., HOSSEINI, M.R., TAGHAVI ZINJENAB, Z., AZIMI, E., 2023. *Significant reduction in collector consumption by implementing ultrafine bubbles in lead and zinc rougher flotation*. Powder Technol. 414, 118096.
- SOBHAY, A., TAO, D., 2013. *High-efficiency nanobubble coal flotation*. Int. J. Coal Prep. Utilization, 33, 242-256.
- WANG, X.H., FORSSBERG, K.E., 1991. *Mechanisms of pyrite flotation with xanthates*. Int. J. Miner. Process. 33, 275-290.
- SEYEDI, M., ABEDI, M., BAHROUDI, A., FERDOWSI, H., 2023. *Geochemical prospectivity of Cu-mineralization through concentration-number fractal modeling and prediction-area plot: a case study in East Iran*. Int. J. Min. Geo-Eng. 57, 159-169.
- TAGHAVI ZINJENAB, Z., AZIMI, E., SHADMAN, M., HOSSEINI, M.R., 2024. *Maximization of ultrafine poly-mineral ore sequential flotation recovery through synergistic effect of conventional and nano-size bubble combination*. J. Mol. Liq. 401, 124698.
- TAGHAVI, F., NOAPARAST, M., POURKARIMI, Z., NAKHAEI, F., 2022. *Comparison of mechanical and column flotation performances on recovery of phosphate slimes in presence of nano-microbubbles*. J. Cent. South Univ. 29, 102-115.
- TAO, D., WU, Z., SOBHAY, A., 2021. *Investigation of nanobubble enhanced reverse anionic flotation of hematite and associated mechanisms*. Powder Technol. 379, 12-25.
- TAO, D., 2022. *Recent advances in fundamentals and applications of nanobubble enhanced froth flotation: A review*. Miner. Eng. 183, 107554.
- ULATOWSKI, K., SOBIESZUK, P., MROZ, T., 2019. *Stability of nanobubbles generated in water using porous membrane system*. Chem, Eng. Process.: Process Intensif. 136, 62-71.
- WEBER, W.J., MORRIS, J.C., 1963. *Kinetics of adsorption on carbon from solution*. J. Sanit. Eng. Div. 89, 31-59.
- WU, Z., TAO, D., MA, G., 2023. *New insights into mechanisms of pyrite flotation enhancement by hydrodynamic cavitation nanobubbles*. Mineral Engineering. 201, 108222.
- YENIAL-ARSLAN, M., JEFFERSON, M., CURTIS-MORAR, C., 2023. *Pathway to prediction of pyrite floatability from copper ore geological domain data*. Minerals. 13, 801.
- ZENG, C., HUANG, K., WANG, C., GONG, Y., HUANG, N., HUANG, X., YANG, H., ZOU, S., ZHONG, H., 2023. *Adsorption kinetic studies of octyl hydroxamic acid on galena surface*. Miner. Eng. 198.
- ZHOU, S., LI, Y., NAZARI, S., BU, X., HASSANZADEH, A., 2022. *An assessment of the role of combined bulk micro-and nano-bubbles in quartz flotation*. Minerals 12, 944.